Supporting Information

Fujita et al. 10.1073/pnas.1406297111

SI Text

1. Models of Spatially Modulated Order in Underdoped Cuprates

The study of the underdoped cuprates has led to proposals of a large number of density-wave ordered states with nontrivial form factors (1–33). Here we provide a unified perspective on these orders, highlighting the key characteristics detected by our observations.

It is useful to begin by considering the following order parameter at the Cu sites $\boldsymbol{r}_i$ and $\boldsymbol{r}_j$ (21, 22),

$$\left\langle c^{\dagger}_{i\alpha} c_{j\alpha} \right\rangle = \sum_{\boldsymbol{Q}} \left[\sum_{\boldsymbol{k}} P(\boldsymbol{k},\boldsymbol{Q}) e^{i\boldsymbol{k}\cdot\left(\boldsymbol{r}_i-\boldsymbol{r}_j\right)} \right] e^{i\boldsymbol{Q}\cdot\left(\boldsymbol{r}_i+\boldsymbol{r}_j\right)/2}, \qquad \textbf{[S1.1]}$$

where $c_{i\alpha}$ annihilates an electron with spin α on a site at position $\boldsymbol{r}_i$. Here the wave vector $\boldsymbol{Q}$ is associated with a modulation in the average coordinate $(\boldsymbol{r}_i+\boldsymbol{r}_j)/2$. The form factor describes the dependence on the relative coordinate $\boldsymbol{r}_i-\boldsymbol{r}_j$. An advantage of the formulation in Eq. **S1.1** is that it provides an efficient characterization of symmetries. The operator identity $<A^{\dagger}> \equiv <A>^{*}$ requires that

$$P^{*}(\boldsymbol{k},\boldsymbol{Q}) = P(\boldsymbol{k},-\boldsymbol{Q}), \qquad \textbf{[S1.2]}$$

whereas

$$P(\boldsymbol{k},\boldsymbol{Q}) = P(-\boldsymbol{k},\boldsymbol{Q}) \qquad \textbf{[S1.3]}$$

if time-reversal symmetry is preserved.

A number of other studies (1, 4, 16, 17, 19) have made the closely related, but distinct parameterization

$$\left\langle c^{\dagger}_{i\alpha} c_{j\alpha} \right\rangle = \sum_{\boldsymbol{Q}} \left[\sum_{\boldsymbol{k}} f(\boldsymbol{k},\boldsymbol{Q}) e^{i\boldsymbol{k}\cdot\left(\boldsymbol{r}_i-\boldsymbol{r}_j\right)} \right] e^{i\boldsymbol{Q}\cdot\boldsymbol{r}_i} \qquad \textbf{[S1.4]}$$

and then considered various ansatzes for the function $f(\boldsymbol{k},\boldsymbol{Q})$. These are clearly related to those for $P(\boldsymbol{k},\boldsymbol{Q})$ by

$$f(\boldsymbol{k},\boldsymbol{Q}) = P\left(\boldsymbol{k}+\frac{\boldsymbol{Q}}{2},\boldsymbol{Q}\right). \qquad \textbf{[S1.5]}$$

It is now clear that the relations **[S1.2]** and **[S1.3]** take a more complex form in terms of $f(\boldsymbol{k},\boldsymbol{Q})$. Also, a d-wave form factor for $f(\boldsymbol{k},\boldsymbol{Q})$ is not equal to a d-wave form factor for $P(\boldsymbol{k},\boldsymbol{Q})$, except at $\boldsymbol{Q}=0$.

We conduct the remainder of the discussion using $P(\boldsymbol{k},\boldsymbol{Q})$ and Eq. **S1.1**. Depending upon the value of $\boldsymbol{Q}$, various crystalline symmetries can also place restrictions on $P(\boldsymbol{k},\boldsymbol{Q})$, and we illustrate this with a few examples.

An early discussion of a state with nontrivial form factors was the "staggered-flux" state (also called the "d-density wave" state), which carries spontaneous staggered currents (2–6). This state has $P(\boldsymbol{k},\boldsymbol{Q})$ nonzero only for $\boldsymbol{Q}=(\pi,\pi)$ and

$$P(\boldsymbol{k},\boldsymbol{Q}) = P_{sf}\left(\sin(k_x)-\sin(k_y)\right) + P'_{sf}\left(\sin(2k_x)-\sin(2k_y)\right)+\cdots, \qquad \textbf{[S1.6]}$$

where P_{sf} and P'_{sf} are constants. All terms on the right-hand side are required by symmetry to be odd under time reversal (i.e., odd in $\boldsymbol{k}$) and odd under the interchange $k_x \leftrightarrow k_y$. In the present notation, therefore, the staggered-flux state is a p-symmetry form factor density wave. Please note that a d-wave form factor in our notation refers to a distinct state below, which should not be confused with the d-density wave of refs. 2–6. With $P(\boldsymbol{k},\boldsymbol{Q})$ nonzero only for $\boldsymbol{Q}=0$ and odd in $\boldsymbol{k}$, we obtain states with spontaneous uniform currents (7).

Another much-studied state is the electronic nematic (8–10). This has $P(\boldsymbol{k},\boldsymbol{Q})$ nonzero only for $\boldsymbol{Q}=0$, with

$$P(\boldsymbol{k},\boldsymbol{Q}) = P_n\left(\cos(k_x)-\cos(k_y)\right) + P'_n\left(\cos(2k_x)-\cos(2k_y)\right)+\cdots. \qquad \textbf{[S1.7]}$$

Now all terms on the right-hand side should be even in $\boldsymbol{k}$ and odd under the interchange $k_x \leftrightarrow k_y$. The ansatz in Eq. **S1.7** also applies to "incommensurate nematics" (21–31), which have $P(\boldsymbol{k},\boldsymbol{Q})$ nonzero only for $\boldsymbol{Q}=(\pm Q,\pm Q)$: These are density waves with $\boldsymbol{Q}$ along the diagonals of the square lattice Brillouin zone and a purely d-wave form factor.

Finally, we turn to the density waves considered in our paper. These have $P(\boldsymbol{k},\boldsymbol{Q})$ nonzero only for $\boldsymbol{Q}=(0,\pm Q)$ and $(\pm Q,0)$. We assume they preserve time reversal, and then the form factor has the general form (22)

$$P(\boldsymbol{k},\boldsymbol{Q}) = P_S + P_{S'}\left(\cos(k_x)+\cos(k_y)\right) + P_D\left(\cos(k_x)-\cos(k_y)\right)+\cdots. \qquad \textbf{[S1.8]}$$

For general incommensurate $\boldsymbol{Q}$, any even function of $\boldsymbol{k}$ is allowed on the right-hand side. Using arguments based upon instabilities of metals with local antiferromagnetic correlations, it was argued in ref. 22 that such a density wave is predominantly d wave, i.e., $|P_D| \gg |P_S|$ and $|P_D| \gg |P_{S'}|$, so that it is very nearly, but not exactly, an incommensurate nematic. The d waveness here is a statement about the physics of the intraunit-cell electronic correlations and is not fully determined by symmetry.

We now make contact with the local observables considered in *SI Text* sections 2 and 3 and as measured by scanning tunneling microscopy (STM). Via the canonical transformation from the two-band to the single-band model of the CuO_2 layer, we can deduce the general relationship

$$\left\langle c^{\dagger}_{i\alpha} c_{j\alpha} + c^{\dagger}_{j\alpha} c_{i\alpha} \right\rangle = \begin{cases} \dfrac{1}{K}\rho(\boldsymbol{r}_{\mathrm{Cu}}) \text{ for } i=j \\ \dfrac{1}{K'}\rho(\boldsymbol{r}_{\mathrm{O}_x}) \text{ for } i,j \text{ n.n along } x \text{ direction} \\ \dfrac{1}{K'}\rho(\boldsymbol{r}_{\mathrm{O}_y}) \text{ for } i,j \text{ n.n along } y \text{ direction.} \end{cases} \qquad \textbf{[S1.9]}$$

Here $\rho(\boldsymbol{r})$ is any density-like (i.e., invariant under time-reversal and spin rotations) observable and K and K' are proportionality constants. Combining **[S1.1]**, **[S1.8]**, and **[S1.9]** we can now write

$$\begin{aligned} \rho(\boldsymbol{r}_{\mathrm{Cu}}) &= 2K\, Re\left\{ \left[\sum_{\boldsymbol{k}} P(\boldsymbol{k},\boldsymbol{Q}) \right] e^{i\boldsymbol{Q}\cdot\boldsymbol{r}_{\mathrm{Cu}}} \right\} \\ &= A_s \cos(\boldsymbol{Q}\cdot\boldsymbol{r}_{\mathrm{Cu}} + \phi_s) \end{aligned} \qquad \textbf{[S1.10]}$$

$$\begin{aligned} \rho(\boldsymbol{r}_{\mathrm{O}_x}) &= 2K'\, Re\left\{ \left[\sum_{\boldsymbol{k}} \cos(k_x) P(\boldsymbol{k},\boldsymbol{Q}) \right] e^{i\boldsymbol{Q}\cdot\boldsymbol{r}_{\mathrm{O}_x}} \right\} \\ &= A_{S'} \cos(\boldsymbol{Q}\cdot\boldsymbol{r}_{\mathrm{O}_x} + \phi_{S'}) + A_D \cos(\boldsymbol{Q}\cdot\boldsymbol{r}_{\mathrm{O}_x} + \phi_D) \end{aligned} \qquad \textbf{[S1.11]}$$

$$\rho(\boldsymbol{r}_{O_y}) = 2K'Re\left\{\left[\sum_k \cos(k_y)P(\boldsymbol{k},\boldsymbol{Q})\right]e^{i\boldsymbol{Q}\cdot\boldsymbol{r}_{O_y}}\right\} = A_{S'}\cos(\boldsymbol{Q}\cdot\boldsymbol{r}_{O_y}+\phi_{S'}) - A_D\cos(\boldsymbol{Q}\cdot\boldsymbol{r}_{O_y}+\phi_D) \quad \textbf{[S1.12]}$$

with $A_S = 2K|P_S|$, $A_{S',D} = K'|P_{S',D}|$, and $\phi_{S,S',D} = \arg(P_{S,S',D})$. Our Fourier transforms of the STM data in Fig. 3 of the main text yield the prefactors in Eqs. **S1.11** and **S1.12**. The observed change in sign between the prefactors demonstrates that $|P_D| \gg |P_{S'}|$ as anticipated in refs. 22–24.

2. Symmetry Decomposition of CuO_2 Intraunit-Cell States

Here we present mathematical details behind the angular momentum form factor organization of density waves on the CuO_2 plane. Among the many ways of organizing density waves in the CuO_2 plane, one is to think of them as a wave on the copper atoms, a wave on the *x*-axis bond oxygen atoms, and a wave on the *y*-axis bond oxygen atoms as presented in Eqs. **S1.10–S1.12**. The results presented in the main text, however, present a compelling case that another organization captures the density wave observed in a remarkably simple way. This way organizes them by angular momentum form factors that we call *s*, *s′* ("extended *s*"), and *d*.

We can think of the angular momentum form factor organization as a modulation of $\boldsymbol{Q}=0$ "waves" whose point group symmetry is well defined, as shown in Fig. S1 *A–C*. The $\boldsymbol{Q}=0$ *s* wave has a density

$$\rho(\boldsymbol{r}_{Cu}) = A_S, \quad \rho(\boldsymbol{r}_{O_x}) = 0, \quad \rho(\boldsymbol{r}_{O_y}) = 0, \quad \textbf{[S2.1]}$$

the $\boldsymbol{Q}=0$ *s′* wave has density

$$\rho(\boldsymbol{r}_{Cu}) = 0, \quad \rho(\boldsymbol{r}_{O_x}) = A_{S'}, \quad \rho(\boldsymbol{r}_{O_y}) = A_{S'}, \quad \textbf{[S2.2]}$$

and the $\boldsymbol{Q}=0$ *d* wave has density

$$\rho(\boldsymbol{r}_{Cu}) = 0, \quad \rho(\boldsymbol{r}_{O_x}) = A_D, \quad \rho(\boldsymbol{r}_{O_y}) = -A_D. \quad \textbf{[S2.3]}$$

The Fourier transforms of these intraunit-cell (IUC) states are shown in Fig. S1 *D–F*. Modulating these waves, we then obtain

$$\rho_S(\boldsymbol{r}) = \begin{cases} A_S\cos(\boldsymbol{Q}\cdot\boldsymbol{r}+\phi_S), & \boldsymbol{r}=\boldsymbol{r}_{Cu}, \\ 0, & \boldsymbol{r}=\boldsymbol{r}_{O_x}, \\ 0, & \boldsymbol{r}=\boldsymbol{r}_{O_y}, \end{cases}$$

$$\rho_{S'}(\boldsymbol{r}) = \begin{cases} 0, & \boldsymbol{r}=\boldsymbol{r}_{Cu}, \\ A_{S'}\cos(\boldsymbol{Q}\cdot\boldsymbol{r}+\phi_{S'}), & \boldsymbol{r}=\boldsymbol{r}_{O_x}, \\ A_{S'}\cos(\boldsymbol{Q}\cdot\boldsymbol{r}+\phi_{S'}), & \boldsymbol{r}=\boldsymbol{r}_{O_y}, \end{cases} \quad \textbf{[S2.4]}$$

$$\rho_D(\boldsymbol{r}) = \begin{cases} 0, & \boldsymbol{r}=\boldsymbol{r}_{Cu}, \\ A_D\cos(\boldsymbol{Q}\cdot\boldsymbol{r}+\phi_D), & \boldsymbol{r}=\boldsymbol{r}_{O_x}, \\ -A_D\cos(\boldsymbol{Q}\cdot\boldsymbol{r}+\phi_D), & \boldsymbol{r}=\boldsymbol{r}_{O_y}, \end{cases}$$

where $\phi_{S,S',D}$ are the phases of each of the density-wave (DW) form factor components. A graphical picture corresponding to these waves is presented in Fig. S2 *A–C*. The Fourier transforms of the three different form factor density waves are presented in Fig. S2 *D–F* and are considered further in *SI Text* section 3. If, for simplicity, we choose $\phi_S = \phi_{S'} = \phi_D = \phi(\boldsymbol{r})$ and allow for spatial disorder of the phase, we arrive at the description used in Eq. **1** of the main text.

Consider now the organization by atomic site. We see that the *s*-wave form factor is just a wave purely on the copper atoms with no weight on the oxygen atoms whereas the *s′*-wave and *d*-wave form factors involve purely the oxygen sites. There is also a curious but practically very important relationship between the *s′*-wave and *d*-wave form factors: In a sense they are like mirror images of each other. For a purely *s′*-form factor DW, taking the sum $\tilde{\rho}_{O_x}(\boldsymbol{q}) + \tilde{\rho}_{O_y}(\boldsymbol{q})$ must recover the Fourier transform of the full *s′*-form factor DW. However, taking the difference $\tilde{\rho}_{O_x}(\boldsymbol{q}) - \tilde{\rho}_{O_y}(\boldsymbol{q})$, we obtain the Fourier transform of the *d*-form factor DW (up to a phase difference $\phi_S - \phi_D$). Similarly, for a density wave with a pure *d*-symmetry form factor, $\tilde{\rho}_{O_x}(\boldsymbol{q}) - \tilde{\rho}_{O_y}(\boldsymbol{q})$ will look like the Fourier transform of a DW with a pure *s′*-symmetry form factor.

Finally, given the above understanding of how the overall electronic structure image [e.g., $R(\boldsymbol{r})$] is built up from its components, there is another possible approach to determining the form factor of any density wave. Phase-resolved Fourier analysis of such an electronic structure image that has not been decomposed into its constituent parts $Cu(\boldsymbol{r})$, $O_x(\boldsymbol{r})$, and $O_y(\boldsymbol{r})$ but remains intact should still reveal the relative magnitude of the three form factors. However, one can show that this is possible only if the three independent DW peaks at $\boldsymbol{Q}$, $\boldsymbol{Q}' = (1,0) \pm \boldsymbol{Q}$ and $\boldsymbol{Q}'' = (0,1) \pm \boldsymbol{Q}$ are well resolved.

3. Predicted Fourier Transform STM Signatures of a *d*-Form Factor DW

As discussed in *SI Text* sections 1 and 2, the projection of a DW into *s*-, *s′*-, and *d*-form factor components is conceptually appealing. However, for the purposes of this section we keep in mind the exigencies of the experimental technique and work in terms of the segregated oxygen sublattice images $O_{x,y}(\boldsymbol{r})$. In terms of the segregated sublattices, a *d*-form factor DW is one for which the DW on the O_x sites is in antiphase with that on the O_y sites. For $\boldsymbol{Q} \neq 0$ ordering the form factor does not uniquely determine the point group symmetry of the DW and hence in general *s*-, *s′*-, and *d*-form factors are free to mix. This section predicts the consequences of a primarily *d*-form factor density wave for $\tilde{O}_{x,y}(\boldsymbol{q})$ and shows its consistency with the data presented in the main text.

To deduce the logical consequences of a *d*-form factor DW for the Fourier transforms of the segregated oxygen site images one can start by constructing the dual real and momentum-space representation of the sublattices:

$$L_{Cu}(\boldsymbol{r}) = \sum_{i,j}\delta(\boldsymbol{r}-\boldsymbol{R}_{i,j}) \Leftrightarrow \tilde{L}_{Cu}(\boldsymbol{q}) = \sum_{h,k}\delta(\boldsymbol{q}-\boldsymbol{G}^{h,k}) \quad \textbf{[S3.1]}$$

$$L_{O_x}(\boldsymbol{r}) = L_{Cu}\left(\boldsymbol{r}-\frac{a_0\hat{\boldsymbol{x}}}{2}\right) \Leftrightarrow \tilde{L}_{O_x}(\boldsymbol{q}) = e^{i\boldsymbol{q}\cdot a_0\hat{\boldsymbol{x}}/2}\tilde{L}_{Cu}(\boldsymbol{q}) \quad \textbf{[S3.2]}$$

$$L_{O_y}(\boldsymbol{r}) = L_{Cu}\left(\boldsymbol{r}-\frac{a_0\hat{\boldsymbol{y}}}{2}\right) \Leftrightarrow \tilde{L}_{O_y}(\boldsymbol{q}) = e^{i\boldsymbol{q}\cdot a_0\hat{\boldsymbol{y}}/2}\tilde{L}_{Cu}(\boldsymbol{q}). \quad \textbf{[S3.3]}$$

The $\{\boldsymbol{R}_{i,j}\}$ are the set of direct lattice vectors of the square lattice with lattice constant a_0 and the $\{\boldsymbol{G}^{h,k}\}$ are the reciprocal lattice vectors. The displacement of the oxygen sublattices from the copper sublattice has the effect of modulating the phase of their Bragg peaks along the direction of displacement with periodicity $4\pi/a_0$ in reciprocal space. This is depicted in Fig. S3*A*.

Using the convolution theorem, a *d*-form factor modulation of the oxygen site density takes on the dual description

$$O_x(\boldsymbol{r}) = L_{O_x}(\boldsymbol{r})\cdot A_{O_x}(\boldsymbol{r}) \Leftrightarrow \tilde{O}_x(\boldsymbol{q}) = \tilde{L}_{O_x}(\boldsymbol{q}) * \tilde{A}_{O_x}(\boldsymbol{q}) \quad \textbf{[S3.4]}$$

$$O_y(\boldsymbol{r}) = L_{O_y}(\boldsymbol{r})\cdot A_{O_y}(\boldsymbol{r}) \Leftrightarrow \tilde{O}_y(\boldsymbol{q}) = \tilde{L}_{O_y}(\boldsymbol{q}) * \tilde{A}_{O_y}(\boldsymbol{q}) \quad \textbf{[S3.5]}$$

$$A_{O_x}(\boldsymbol{r}) = -A_{O_y}(\boldsymbol{r}) = A(\boldsymbol{r}) \Leftrightarrow \tilde{A}_{O_x}(\boldsymbol{q}) = -\tilde{A}_{O_y}(\boldsymbol{q}) = A(\boldsymbol{q}). \quad \textbf{[S3.6]}$$

The functions $O_{x,y}(\boldsymbol{r})$ are the segregated oxygen sublattice images. The $A_{O_{x,y}}(\boldsymbol{r})$ are continuous functions that when multiplied

by the sublattice functions yield density waves in antiphase on the separate oxygen sublattices (Fig. S3*B*). Fig. S3*C* shows their Fourier transforms $\tilde{A}_{O_{x,y}}(\boldsymbol{q})$. Note that $A(\boldsymbol{r})$ may contain arbitrary amplitude and overall phase disorder but remain *d* wave as long as the relative phase relation in Eq. **S3.6** is maintained.

As shown in Fig. S4*A*, the convolutions in Eqs. **S3.4** and **S3.5** create an image of $\tilde{A}_{O_{x,y}}(\boldsymbol{q})$ at each reciprocal lattice vector that sums to form the total convolution. Labeling the convolution image due to the reciprocal lattice vector (h,k) in the *x* sublattice $\tilde{O}_x^{h,k}(\boldsymbol{q})$,

$$\tilde{O}_x(\boldsymbol{q}) = \sum_{h,k} \tilde{O}_x^{h,k}(\boldsymbol{q}) = \sum_{h,k} e^{i\boldsymbol{G}^{h,k}\cdot a_0\hat{\boldsymbol{x}}/2}\tilde{A}_{O_x}\left(\boldsymbol{q}-\boldsymbol{G}^{h,k}\right). \qquad \textbf{[S3.7]}$$

In creating the (h,k) convolution image, the phase of the sublattice Bragg peak at $\boldsymbol{G}^{h,k}$ and that of the form factor $\tilde{A}_{O_x}(\boldsymbol{q})$ must be added:

$$\arg\left\{\tilde{O}_x^{h,k}(\boldsymbol{q})\right\} = \arg\left\{\tilde{A}_{O_x}\left(\boldsymbol{q}-\boldsymbol{G}^{h,k}\right)\right\} + \arg\left\{e^{i\boldsymbol{G}^{h,k}\cdot a_0\hat{\boldsymbol{x}}/2}\right\}. \qquad \textbf{[S3.8]}$$

Thus, it follows immediately that

$$\tilde{O}_x^{0,0} = \tilde{A}(\boldsymbol{q}), \quad \tilde{O}_y^{0,0} = -\tilde{A}(\boldsymbol{q}) \qquad \textbf{[S3.9]}$$

$$\tilde{O}_x^{1,0} = -\tilde{A}(\boldsymbol{q}), \quad \tilde{O}_y^{1,0} = -\tilde{A}(\boldsymbol{q}) \qquad \textbf{[S3.10]}$$

$$\tilde{O}_x^{0,1} = \tilde{A}(\boldsymbol{q}), \quad \tilde{O}_y^{0,1} = \tilde{A}(\boldsymbol{q}) \qquad \textbf{[S3.11]}$$

and hence

$$\tilde{O}_x^{0,0} + \tilde{O}_y^{0,0} = 0, \qquad \tilde{O}_x^{0,0} - \tilde{O}_y^{0,0} = 2\tilde{A}(\boldsymbol{q}) \qquad \textbf{[S3.12]}$$

$$\tilde{O}_x^{1,0} + \tilde{O}_y^{1,0} = -2\tilde{A}(\boldsymbol{q}), \quad \tilde{O}_x^{1,0} - \tilde{O}_y^{1,0} = 0 \qquad \textbf{[S3.13]}$$

$$\tilde{O}_x^{0,1} + \tilde{O}_y^{0,1} = 2\tilde{A}(\boldsymbol{q}), \quad \tilde{O}_x^{0,1} - \tilde{O}_y^{0,1} = 0. \qquad \textbf{[S3.14]}$$

A direct consequence of a *d*-form factor is that in $\tilde{O}_x(\boldsymbol{q}) + \tilde{O}_y(\boldsymbol{q})$ the amplitude of the convolution image at (0,0) is canceled exactly whereas those at the (±1, 0) and (0, ±1) points are enhanced as illustrated in Fig. S4 *B* and *C*. The converse is true for $\tilde{O}_x(\boldsymbol{q}) - \tilde{O}_y(\boldsymbol{q})$. This holds for any *d*-wave modulation in the presence of arbitrary amplitude and overall phase disorder.

Fig. S2 *D*–*F* shows Fourier transforms of different form factor density waves in the CuO_2 plane. A *d*-form factor density wave has modulations only on the oxygen sites and hence its contribution to the full Fourier transform is contained entirely within $\tilde{O}_x(\boldsymbol{q}) + \tilde{O}_y(\boldsymbol{q})$. From Eqs. **S3.12**–**S3.14** we must conclude that for density waves with principal wave vectors that lie within the first Brillouin zone, $\tilde{\rho}_D(\boldsymbol{q})$ (Fig. S2*F*) will exhibit an absence of peaks at these wave vectors in the first Brillouin zone. For $\tilde{\rho}_S(\boldsymbol{q})$ (Fig. S2*D*) and $\tilde{\rho}_{S'}(\boldsymbol{q})$ (Fig. S2*E*) we may conclude that they will be present, using similar arguments.

Empirically (main text Figs. 3 and 4), our data contain modulations at two wave vectors $\boldsymbol{Q}_x = (Q,0)$ and $\boldsymbol{Q}_y = (0,Q)$ with $Q \sim 1/4$ but with a great deal of fluctuation in the spatial phase of the DW (34). However, it would be improper to conclude from this that we observe a bidirectional *d*-form factor DW, often termed the "checkerboard" modulation. The strong disorder of the density modulations in $Bi_2Sr_2CaCu_2O_{8+x}$ (BSCCO) and $Ca_{2-x}Na_xCuO_2Cl_2$ (NaCCOC) is apparent in the real-space images presented in Fig. 2 of the main text and *SI Text* section 5. Random charge disorder can have the effect of taking a clean system with an instability toward unidirectional ("stripe") ordering and produce domains of unidirectional order that align with the local anisotropy. Conversely, a clean system with an instability toward bidirectional (checkerboard) ordering may have local anisotropy imbued upon it by disorder.

Although the wave vector(s) of the underlying instability of the copper oxide plane to DW ordering are of theoretical interest, any *d*-form factor DW containing two wave vectors $\boldsymbol{Q}_x$ and $\boldsymbol{Q}_y$ can be described by

$$A(\boldsymbol{r}) = Re\left[e^{i\boldsymbol{Q}_x\cdot\boldsymbol{r}}\cdot H_x(\boldsymbol{r})\right] + Re\left[e^{i\boldsymbol{Q}_y\cdot\boldsymbol{r}}\cdot H_y(\boldsymbol{r})\right] \qquad \textbf{[S3.15]}$$

$$\tilde{A}(\boldsymbol{q}) = \frac{1}{2}\left[\tilde{H}_x(\boldsymbol{q}-\boldsymbol{Q}_x) + \tilde{H}_x^*(\boldsymbol{q}+\boldsymbol{Q}_x) + \tilde{H}_y(\boldsymbol{q}-\boldsymbol{Q}_y) + \tilde{H}_y^*(\boldsymbol{q}+\boldsymbol{Q}_y)\right]. \qquad \textbf{[S3.16]}$$

The complex valued functions $H_{x,y}(\boldsymbol{r})$ locally modulate the amplitude and phase of the density wave and hence encode its disorder. The problem now reduces to performing the convolutions contained in Eqs. **S3.4**–**S3.6**.

For the specific example of $\boldsymbol{Q}_x \approx (1/4, 0)$ and $\boldsymbol{Q}_y \approx (0, 1/4)$ considered in our study the primarily *d*-wave form factor requires that the peaks at $\pm\boldsymbol{Q}_x$ and $\pm\boldsymbol{Q}_y$ present in both $\tilde{O}_x(\boldsymbol{q})$ and $\tilde{O}_y(\boldsymbol{q})$ must cancel exactly in $\tilde{O}_x(\boldsymbol{q}) + \tilde{O}_y(\boldsymbol{q})$ and be enhanced in $\tilde{O}_x(\boldsymbol{q}) - \tilde{O}_y(\boldsymbol{q})$. Conversely the peaks at $\boldsymbol{Q}' = (1,0) \pm \boldsymbol{Q}_{x,y}$ and $\boldsymbol{Q}'' = (0,1) \pm \boldsymbol{Q}_{x,y}$ will be enhanced in $\tilde{O}_x(\boldsymbol{q}) + \tilde{O}_y(\boldsymbol{q})$ but will cancel exactly in $\tilde{O}_x(\boldsymbol{q}) - \tilde{O}_y(\boldsymbol{q})$. These are necessary consequences of a DW with a primarily *d*-wave form factor. This is discussed in the main text and in accord with the observations in Figs. 2–4 of the main text.

4. Sublattice Phase Definition: Lawler–Fujita Algorithm

Consider an atomically resolved STM topograph, $T(\boldsymbol{r})$, with tetragonal symmetry where two orthogonal wave vectors generate the atomic corrugations. These are centered at the first reciprocal unit-cell Bragg wave vectors $\boldsymbol{Q}_a = (Q_{ax}, Q_{ay})$ and $\boldsymbol{Q}_b = (Q_{bx}, Q_{by})$ with $\boldsymbol{a}$ and $\boldsymbol{b}$ being the unit-cell vectors. Schematically, the ideal topographic image can be written as

$$T(\boldsymbol{r}) = T_0[\cos(\boldsymbol{Q}_a\cdot\boldsymbol{r}) + \cos(\boldsymbol{Q}_b\cdot\boldsymbol{r})]. \qquad \textbf{[S4.1]}$$

In spectroscopic imaging STM, the $T(\boldsymbol{r})$ and its simultaneously measured spectroscopic current map, $I(\boldsymbol{r},V)$, and differential conductance map, $g(\boldsymbol{r},V)$, are specified by measurements on a square array of pixels with coordinates labeled $\boldsymbol{r} = (x,y)$. The power spectral-density (PSD) Fourier transform of $T(\boldsymbol{r})$, $|\tilde{T}(\boldsymbol{q})|^2$, where $\tilde{T}(\boldsymbol{q}) = Re\tilde{T}(\boldsymbol{q}) + iIm\tilde{T}(\boldsymbol{q})$, then exhibits two distinct peaks at $\boldsymbol{q} = \boldsymbol{Q}_a$ and $\boldsymbol{Q}_b$.

In an actual experiment, $T(\boldsymbol{r})$ suffers picometer-scale distortions from the ideal representation in [**S4.1**] according to a slowly varying "displacement field," $\boldsymbol{u}(\boldsymbol{r})$. The same distortion is also found in the spectroscopic data. Thus, a topographic image, including distortions, is schematically written as

$$T(\boldsymbol{r}) = T_0[\cos(\boldsymbol{Q}_a\cdot(\boldsymbol{r}+\boldsymbol{u}(\boldsymbol{r}))) + \cos(\boldsymbol{Q}_b\cdot(\boldsymbol{r}+\boldsymbol{u}(\boldsymbol{r})))]. \qquad \textbf{[S4.2]}$$

Then, to remove the effects of $\boldsymbol{u}(\boldsymbol{r})$ requires an affine transformation at each point in space.

To begin, define the local phase of the atomic cosine components, at a given point $\boldsymbol{r}$, as

$$\begin{aligned}\varphi_a(\boldsymbol{r}) &= \boldsymbol{Q}_a\cdot\boldsymbol{r} + \theta_a(\boldsymbol{r})\\ \varphi_b(\boldsymbol{r}) &= \boldsymbol{Q}_b\cdot\boldsymbol{r} + \theta_b(\boldsymbol{r}),\end{aligned} \qquad \textbf{[S4.3]}$$

which recasts Eq. **S4.2** as

$$T(\boldsymbol{r}) = T_0[\cos(\varphi_a(\boldsymbol{r})) + \cos(\varphi_b(\boldsymbol{r}))], \qquad \textbf{[S4.4]}$$

where $\theta_i(\boldsymbol{r}) = \boldsymbol{Q}_i \cdot \boldsymbol{u}(\boldsymbol{r})$ is additional phase generated by the displacement field. If there were no distortions and the $T(\boldsymbol{r})$ image were perfectly periodic, then $\theta_i(\boldsymbol{r})$ would be constant. From this perspective, the two-dimensional lattice in [**S4.4**] is a function of phase alone. For example, the apex of every atom in the topographic image has the same phase, 0 (mod 2π) regardless of where it is in the image. When viewed in the $\boldsymbol{r}$ coordinates, the distance between such points of equal phase in the "perfect" lattice and the distorted lattice is not the same. The problem of correcting $T(\boldsymbol{r})$ then reduces to finding a transformation to map the distorted lattice onto the perfect one, using the phase information $\varphi_i(\boldsymbol{r})$. This is equivalent to finding a set of local transformations that makes $\theta_a(\boldsymbol{r})$ and $\theta_b(\boldsymbol{r})$ constant over all space; call them $\overline{\theta}_a$ and $\overline{\theta}_b$, respectively.

Let $\boldsymbol{r}$ be a point on the unprocessed $T(\boldsymbol{r})$ and let $\tilde{\boldsymbol{r}}$ be the point of equal phase on the perfect lattice periodic image, which needs to be determined. This produces a set of equivalency relations

$$\begin{aligned} \boldsymbol{Q}_a \cdot \boldsymbol{r} + \theta_a(\boldsymbol{r}) &= \boldsymbol{Q}_a \cdot \tilde{\boldsymbol{r}} + \overline{\theta}_a \\ \boldsymbol{Q}_b \cdot \boldsymbol{r} + \theta_b(\boldsymbol{r}) &= \boldsymbol{Q}_b \cdot \tilde{\boldsymbol{r}} + \overline{\theta}_b. \end{aligned} \qquad \textbf{[S4.5]}$$

Solving for $\tilde{\boldsymbol{r}} = (\tilde{x}, \tilde{y})$ and then assigning the values of the topographic image at $\boldsymbol{r} = (x, y)$, $T(\boldsymbol{r})$, to $\tilde{\boldsymbol{r}}$ produces the perfect lattice. To solve for $\tilde{\boldsymbol{r}}$ rewrite [**S4.5**] in matrix form

$$\boldsymbol{Q}\begin{pmatrix} \tilde{x} \\ \tilde{y} \end{pmatrix} = \boldsymbol{Q}\begin{pmatrix} x \\ y \end{pmatrix} - \begin{pmatrix} \overline{\theta}_a - \theta_a(\boldsymbol{r}) \\ \overline{\theta}_b - \theta_b(\boldsymbol{r}) \end{pmatrix}, \qquad \textbf{[S4.6]}$$

where

$$\boldsymbol{Q} = \begin{pmatrix} Q_{ax} & Q_{ay} \\ Q_{bx} & Q_{by} \end{pmatrix}. \qquad \textbf{[S4.7]}$$

Because $\boldsymbol{Q}_a$ and $\boldsymbol{Q}_b$ are orthogonal, $\boldsymbol{Q}$ is invertible, allowing one to solve for the displacement field $\boldsymbol{u}(\boldsymbol{r})$ that maps $\boldsymbol{r}$ to $\tilde{\boldsymbol{r}}$:

$$\boldsymbol{u}(\boldsymbol{r}) = \boldsymbol{Q}^{-1}\begin{pmatrix} \overline{\theta}_a - \theta_a(\boldsymbol{r}) \\ \overline{\theta}_b - \theta_b(\boldsymbol{r}) \end{pmatrix}. \qquad \textbf{[S4.8]}$$

In practice, we use the convention $\overline{\theta}_i = 0$, which generates a perfect lattice with an atomic peak centered at the origin. This is equivalent to setting to zero the imaginary component of the Bragg peaks in the Fourier transform.

Of course, to use the transformation in [**S4.6**] one must first extract $\theta_i(\boldsymbol{r})$ from the topographic data. This is accomplished by using a computational lock-in technique in which the topograph, $T(\boldsymbol{r})$, is multiplied by reference sine and cosine functions with periodicity set by $\boldsymbol{Q}_a$ and $\boldsymbol{Q}_b$. The resulting four images are filtered to retain only the $\boldsymbol{q}$-space regions within a radius $\delta q = 1/\lambda$ of the four Bragg peaks; the magnitude of λ is chosen to capture only the relevant image distortions. This procedure results in retaining the local phase information $\theta_a(\boldsymbol{r}), \theta_b(\boldsymbol{r})$ that quantifies the local displacements from perfect periodicity:

$$Y_i(\boldsymbol{r}) = \sin\theta_i(\boldsymbol{r}), \qquad X_i(\boldsymbol{r}) = \cos\theta_i(\boldsymbol{r}). \qquad \textbf{[S4.9]}$$

Dividing the appropriate pair of images allows one to extract $\theta_i(\boldsymbol{r})$:

$$\theta_i(\boldsymbol{r}) = \tan^{-1}\frac{Y_i(\boldsymbol{r})}{X_i(\boldsymbol{r})}. \qquad \textbf{[S4.10]}$$

5. Data Analysis

In Fig. S5 we show the power spectral-density Fourier transform analysis $|\widetilde{Cu}(\boldsymbol{q})|^2$ and $|(\tilde{O}_x(\boldsymbol{q}) + \tilde{O}_y(\boldsymbol{q}))/2|^2$, yielding the s-form factor magnitude S and the s'-form factor magnitude S', respectively. These are the equivalent result for $|(\tilde{O}_x(\boldsymbol{q}) - \tilde{O}_y(\boldsymbol{q}))/2|^2$, which is shown in Fig. 4*A* of the main text. The measured values S and S' are plotted along the dashed lines through $\boldsymbol{Q}$ together with the value D in Fig. 4*B* of the main text.

In Fig. 4*D* of the main text, we show the 2D histogram of the amplitude difference and the phase difference between $O_x(\boldsymbol{r})$ and $O_y(\boldsymbol{r})$. To construct this, first, the magnitude and the phase associated only with $\boldsymbol{Q}_x \sim (1/4,0)$ and $\boldsymbol{Q}_y \sim (0,1/4)$ are calculated by using the Fourier filtration in $O_x(\boldsymbol{r})$ and $O_y(\boldsymbol{r})$,

$$\tilde{O}_\alpha(\boldsymbol{r}, \boldsymbol{q}) = \int d\boldsymbol{R} O_\alpha(\boldsymbol{R}) e^{i\boldsymbol{q}\cdot\boldsymbol{R}} e^{-\left(|\boldsymbol{r}-\boldsymbol{R}|^2/2\Lambda^2\right)} \frac{1}{2\pi\Lambda^2}, \qquad \textbf{[S5.1]}$$

where α, $\beta = x, y$, and Λ is the averaging length, ~30 Å.

For $\boldsymbol{q} = \boldsymbol{Q}_\beta$, amplitudes and phases are given by

$$\left|\tilde{O}_\alpha(\boldsymbol{r}, \boldsymbol{Q}_\beta)\right| = \sqrt{\left[Re\tilde{O}_\alpha(\boldsymbol{r}, \boldsymbol{Q}_\beta)\right]^2 + \left[Im\tilde{O}_\alpha(\boldsymbol{r}, \boldsymbol{Q}_\beta)\right]^2}, \qquad \textbf{[S5.2]}$$

$$\arg\left[\tilde{O}_\alpha(\boldsymbol{r}, \boldsymbol{Q}_\beta)\right] = \tan^{-1}\left(\frac{Im\tilde{O}_\alpha(\boldsymbol{r}, \boldsymbol{Q}_\beta)}{Re\tilde{O}_\alpha(\boldsymbol{r}, \boldsymbol{Q}_\beta)}\right). \qquad \textbf{[S5.3]}$$

Next, the normalized amplitude difference and the phase difference are then defined by

$$\frac{\left|\tilde{O}_x(\boldsymbol{r}, \boldsymbol{Q}_\beta)\right| - \left|\tilde{O}_y(\boldsymbol{r}, \boldsymbol{Q}_\beta)\right|}{\left|\tilde{O}_x(\boldsymbol{r}, \boldsymbol{Q}_\beta)\right| + \left|\tilde{O}_y(\boldsymbol{r}, \boldsymbol{Q}_\beta)\right|}, \qquad \textbf{[S5.4]}$$

$$\left|\arg\left[\tilde{O}_x(\boldsymbol{r}, \boldsymbol{Q}_\beta)\right] - \arg\left[\tilde{O}_y(\boldsymbol{r}, \boldsymbol{Q}_\beta)\right]\right|. \qquad \textbf{[S5.5]}$$

Finally, using [**S5.4**] and [**S5.5**] we obtain a 2D histogram for both $\boldsymbol{Q}_x$ and $\boldsymbol{Q}_y$, independently, and then take the sum of them to construct a single distribution containing the information for both $\boldsymbol{Q}_x$ and $\boldsymbol{Q}_y$.

In Fig. S6 we show the measured $R(\boldsymbol{r})$ (subset of main text Fig. 2*A* is presented because the original field of view is so large that the DW is no longer visible clearly) and its segregation into three site-specific images $Cu(\boldsymbol{r})$, $O_x(\boldsymbol{r})$, and $O_y(\boldsymbol{r})$ as described in the main text. With the origin set at a Cu site, Fig. S7 then shows the three complex valued Fourier transform images derived from Fig. 2*A*: $\widetilde{Cu}(\boldsymbol{q}) \equiv Re\widetilde{Cu}(\boldsymbol{q}) + iIm\widetilde{Cu}(\boldsymbol{q})$, $\tilde{O}_x(\boldsymbol{q}) \equiv Re\tilde{O}_x(\boldsymbol{q}) + iIm\tilde{O}_x(\boldsymbol{q})$, and $\tilde{O}_y(\boldsymbol{q}) \equiv Re\tilde{O}_y(\boldsymbol{q}) + iIm\tilde{O}_y(\boldsymbol{q})$. This type of sublattice-phase–resolved Fourier analysis that we introduce in this paper provides the capability to measure the relative phase of different sites with each CuO_2 unit cell. Fig. S6*A*, *Inset* shows the difference between the real component of Bragg intensity for (1,0) and (0,1) peaks in the Fourier transforms of the electronic structure images before sublattice segregation. It is this difference that was originally used to determine the d-form factor of the intraunit-cell nematic state. Figs. S8 and S9 present the corresponding data and analysis for NaCCOC.

Fig. S10 compares the analysis of $Z(\boldsymbol{r},|E|) = g(\boldsymbol{r},E)/g(\boldsymbol{r},-E)$ (E = 150 meV) between BSCCO (Fig. S10 *A–D*) and NaCCOC (Fig. S10 *E–H*). Both $Z(\boldsymbol{r},|E|)$ are segregated into three site-specific images $Cu(\boldsymbol{r})$, $O_x(\boldsymbol{r})$, and $O_y(\boldsymbol{r})$ first. The analysis is then presented in terms of their complex Fourier transforms $Re\tilde{O}_x(\boldsymbol{q})$ and $Re\tilde{O}_y(\boldsymbol{q})$ as described in the main text. One can see directly that the phenomena are extremely similar for both compounds, in terms of $Re\tilde{O}_x(\boldsymbol{q})$, $Re\tilde{O}_y(\boldsymbol{q})$, and $Re\tilde{O}_x(\boldsymbol{q}) \pm Re\tilde{O}_y(\boldsymbol{q})$. Moreover, they are in excellent agreement with expectations for a d-form

factor DW (*d*FF-DW) in Fig. S4 *B* and *C*. Thus, in the main text, we present analysis of $Z(\boldsymbol{r},E = 150\ \text{meV})$ on an equivalent basis to $R(\boldsymbol{r},E = 150\ \text{meV})$ when deriving $\tilde{O}_x(\boldsymbol{q}) \equiv Re\tilde{O}_x(\boldsymbol{q}) + iIm\tilde{O}_x(\boldsymbol{q})$ and $\tilde{O}_y(\boldsymbol{q}) \equiv Re\tilde{O}_y(\boldsymbol{q}) + iIm\tilde{O}_y(\boldsymbol{q})$ for Fig. 3 *E*–*H* of the main text.

1. Nayak C (2000) Density–wave states of nonzero angular momentum. *Phys Rev B* 62(8): 4880–4889.
2. Affleck I, Marston JB (1988) Large-*n* limit of the Heisenberg-Hubbard model: Implications for high-T_c superconductors. *Phys Rev B* 37(7):3774–3777.
3. Wang Z, Kotliar G, Wang X-F (1990) Flux-density wave and superconducting instability of the staggered-flux phase. *Phys Rev B* 42(13):8690–8693.
4. Chakravarty S, Laughlin RB, Morr DK, Nayak C (2001) Hidden order in the cuprates. *Phys Rev B* 63(9):094503-1–094503-10.
5. Lee PA, Nagaosa N, Wen X-G (2006) Doping a Mott insulator: Physics of high-temperature superconductivity. *Rev Mod Phys* 78(17):17–85.
6. Laughlin RB (2014) Hartree-Fock computation of the high-T_c cuprate phase diagram. *Phys Rev B* 89(3):035134-1–035134-19.
7. Simon ME, Varma CM (2002) Detection and implications of a time-reversal breaking state in underdoped cuprates. *Phys Rev Lett* 89(24):247003-1–247003-4.
8. Kivelson SA, Fradkin E, Emery VJ (1998) Electronic liquid-crystal phases of a doped Mott insulator. *Nature* 393(6685):550–553.
9. Yamase H, Kohno H (2002) Instability toward formation of quasi-one-dimensional Fermi surface in two-dimensional *t-J* model. *J Phys Soc Jpn* 69:2151–2157.
10. Halboth CJ, Metzner W (2000) *d*-wave superconductivity and Pomeranchuk instability in the two-dimensional Hubbard model. *Phys Rev Lett* 85(24):5162–5165.
11. Sachdev S, Read N (1991) Large N expansion for frustrated and doped quantum antiferromagnets. *Int J Mod Phys B* 5(1):219–249.
12. Vojta M, Sachdev S (1999) Charge order, superconductivity, and a global phase diagram of doped antiferromagnets. *Phys Rev Lett* 83(19):3916–3919.
13. Vojta M, Zhang Y, Sachdev S (2000) Competing orders and quantum criticality in doped antiferromagnets. *Phys Rev B* 62(10):6721–6744.
14. Vojta M (2002) Superconducting charge-ordered states in cuprates. *Phys Rev B* 66(10): 104505-1–104505-5.
15. Sachdev S (2003) Order and quantum phase transitions in the cuprate superconductors. *Rev Mod Phys* 75(3):913–932.
16. Vojta M, Rösch O (2008) Superconducting *d*-wave stripes in cuprates: Valence bond order coexisting with nodal quasiparticles. *Phys Rev B* 77(9):094504-1–094504-8.
17. Li J-X, Wu C-Q, Lee D-H (2006) Checkerboard charge density wave and pseudogap of high-T_c cuprate. *Phys Rev B* 74(18):184515-1–184515-6.
18. Davis JC, Lee D-H (2013) Concepts relating magnetic interactions, intertwined electronic orders, and strongly correlated superconductivity. *Proc Natl Acad Sci USA* 110(44):17623–17630.
19. Seo K, Chen H-D, Hu J (2007) *d*-wave checkerboard order in cuprates. *Phys Rev B* 76(2): 020511-1–020511-4.
20. Newns DM, Tsuei CC (2007) Fluctuating Cu-O-Cu bond model of high-temperature superconductivity. *Nat Phys* 3(3):184–191.
21. Metlitski MA, Sachdev S (2010) Quantum phase transitions of metals in two spatial dimensions. II. Spin density wave order. *Phys Rev B* 82(7):075128-1–075128-30.
22. Sachdev S, La Placa R (2013) Bond order in two-dimensional metals with antiferromagnetic exchange interactions. *Phys Rev Lett* 111(2):027202-1–027202-5.
23. Allais A, Bauer J, Sachdev S (2014) Bond order instabilities in a correlated two-dimensional metal. arXiv:1402.4807.
24. Allais A, Bauer J, Sachdev S (2014) Auxiliary-boson and DMFT studies of bond ordering instabilities of *t-J-V* models on the square lattice. arXiv:1402.6311.
25. Holder T, Metzner W (2012) Incommensurate nematic fluctuations in two-dimensional metals. *Phys Rev B* 85(16):165130-1–165130-7.
26. Husemann C, Metzner W (2012) Incommensurate nematic fluctuations in the two-dimensional Hubbard model. *Phys Rev B* 86(8):085113-1–085113-7.
27. Bejas M, Greco A, Yamase H (2012) Possible charge instabilities in two-dimensional doped Mott insulators. *Phys Rev B* 86(22):224509-1–224509-12.
28. Efetov KB, Meier H, Pépin C (2013) Pseudogap state near a quantum critical point. *Nat Phys* 9(7):442–446.
29. Kee H-Y, Puetter CM, Stroud D (2013) Transport signatures of electronic-nematic stripe phases. *J Phys Condens Matter* 25(20):202201-1–202201-6.
30. Bulut S, Atkinson WA, Kampf AP (2013) Spatially modulated electronic nematicity in the three-band model of cuprate superconductors. *Phys Rev B* 88(15):155132-1–155132-13.
31. Sau JD, Sachdev S (2014) Mean-field theory of competing orders in metals with antiferromagnetic exchange interactions. *Phys Rev B* 89(7):075129-1–075129-11.
32. Meier H, Pépin C, Einenkel M, Efetov KB (2013) Cascade of phase transitions in the vicinity of a quantum critical point. *Phys Rev B* 89(19):195115.
33. Wang Y, Chubukov AV (2014) Charge order and loop currents in hole-doped cuprates. arXiv:1401.0712.
34. Hamidian M, et al. (2012) Picometer registration of zinc impurity states in $Bi_2Sr_2CaCu_2O_{8+\delta}$ for phase determination in intra-unit-cell Fourier transform STM. *New J Phys* 14(5): 053017-1–053017-13.

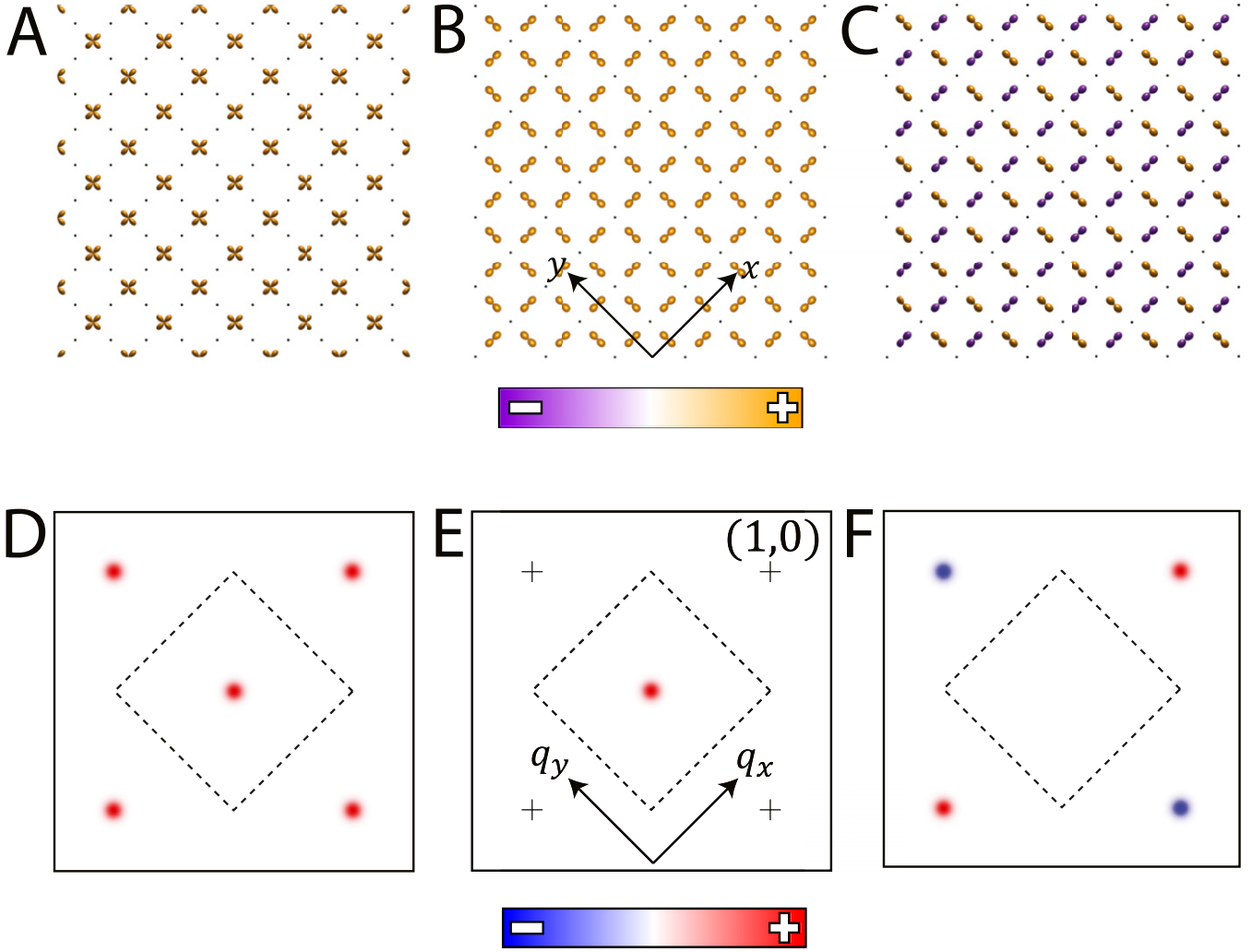

Fig. S1. Intraunit-cell electronic structure symmetry in the CuO_2 plane. (*A*) Schematic of uniform density on the Cu atoms (*s* symmetry). The inactive O sites are now indicated by black dots. (*B*) Schematic of uniform density on the O atoms (also an *s* symmetry referred to here as extended-*s* or *s*′ symmetry). The inactive Cu sites are indicated by black dots. (*C*) Schematic pattern with opposite-sign density on O_x and O_y (*d* symmetry). The inactive Cu sites are indicated by black dots. (*D*) Real component of Fourier transform of the *s*-symmetry IUC patterns derived only from Cu sublattice in *A* and with no DW modulation. The Bragg peaks have the same sign, indicating the IUC states have *s* symmetry. (*E*) Real component of Fourier transform of the *s*′-symmetry IUC patterns derived only from O_x and O_y sublattices in *B* and with no DW. The Bragg peaks are no longer within the CuO_2 reciprocal unit cell (RUC). (*F*) Real component of Fourier transform of the *d*-symmetry IUC patterns derived only from O_x and O_y sublattices as shown in *C* and with no DW modulation. The Bragg peaks now have the opposite sign, indicating the IUC states have *d* symmetry.

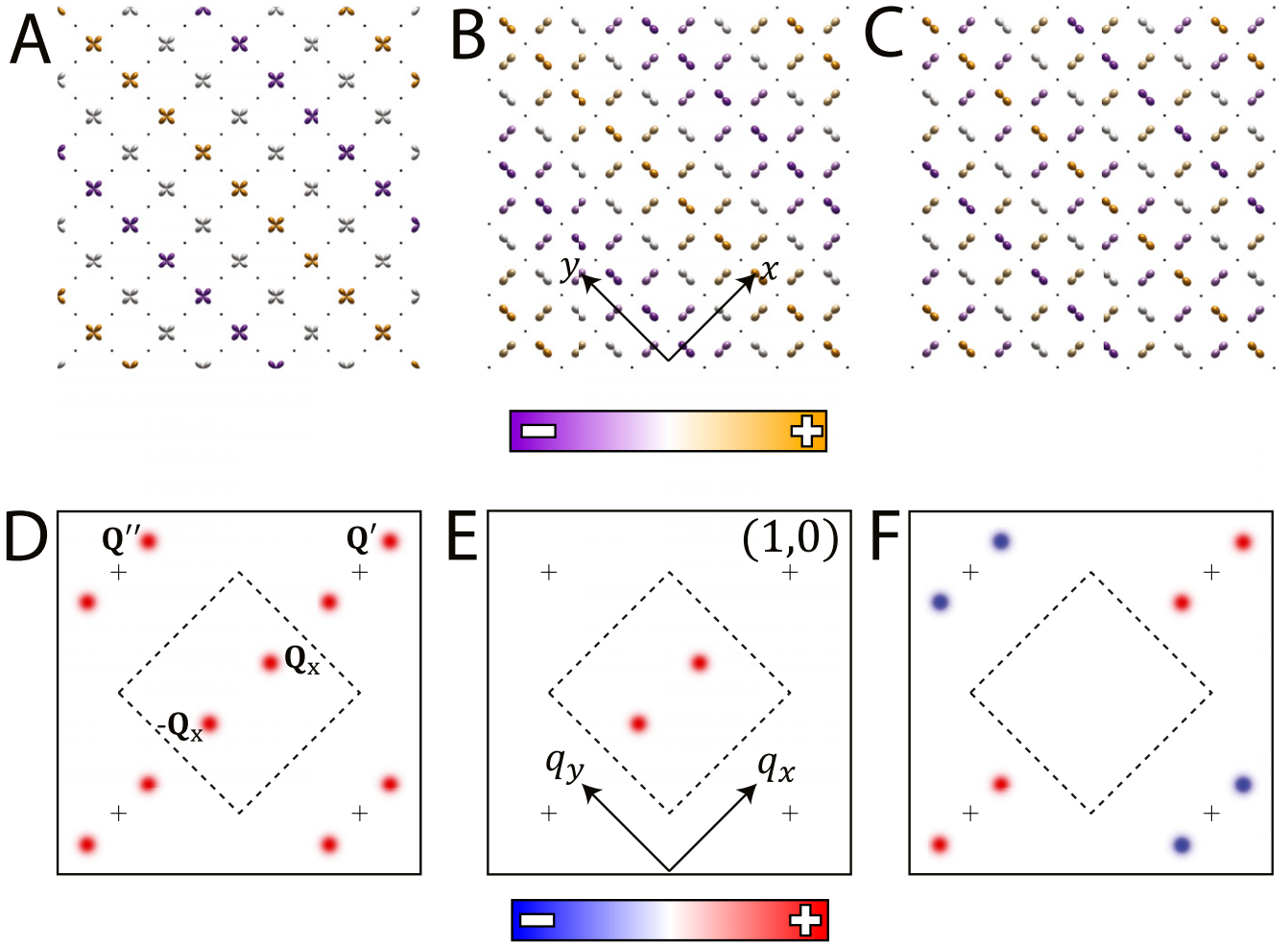

Fig. S2. Types of CuO_2 intraunit-cell density waves. (*A*) Spatial modulation with wave vector $\boldsymbol{Q} = (Q,0)$ of the *s*-symmetry IUC patterns in Fig. S1*A* is described by $\rho_S(\boldsymbol{r}) = S(\boldsymbol{r})\cos(\boldsymbol{Q}\cdot\boldsymbol{r})$; only Cu sites are active. The inactive O sites are indicated by black dots. (*B*) Spatial modulation with wave vector $\boldsymbol{Q}$ of the patterns in Fig. S1*B* described by $\rho_{S'}(\boldsymbol{r}) = S'(\boldsymbol{r})\cos(\boldsymbol{Q}\cdot\boldsymbol{r})$; only O_x and O_y sites are active but they are always equivalent within each unit cell. The inactive Cu sites are indicated by black dots. (*C*) Spatial modulation with wave vector $\boldsymbol{Q}$ of the patterns in Fig. S1*C* described by $\rho_D(\boldsymbol{r}) = D(\boldsymbol{r})\cos(\boldsymbol{Q}\cdot\boldsymbol{r})$; only O_x and O_y sites are relevant but now they are always inequivalent and indeed π out of phase. (*D*) $Re\tilde{\rho}_S(\boldsymbol{q})$, the real component of Fourier transform of the pattern in *A*. For this *s*-form factor DW, the DW satellites of inequivalent Bragg peaks $\boldsymbol{Q}'$ and $\boldsymbol{Q}''$ exhibit the same sign. (*E*) $Re\tilde{\rho}_{S'}(\boldsymbol{q})$, the real component of Fourier transform of the pattern in *B*. For this *s*-form factor DW, the peaks at $\boldsymbol{Q}$ are clear and the actual Bragg peaks of *B* are outside the RUC of CuO_2. (*F*) $Re\tilde{\rho}_D(\boldsymbol{q})$, the real component of Fourier transform of the pattern in *C*. For this *d*-form factor DW, the DW Bragg-satellite peaks at $\boldsymbol{Q}'$ and $\boldsymbol{Q}''$ exhibit opposite sign. More profoundly, because they are out of phase by π the contributions of O_x and O_y sites in each unit cell cancel, resulting in the disappearance of the DW modulation peaks $\boldsymbol{Q}$ within the Brillouin zone (BZ) (dashed box).

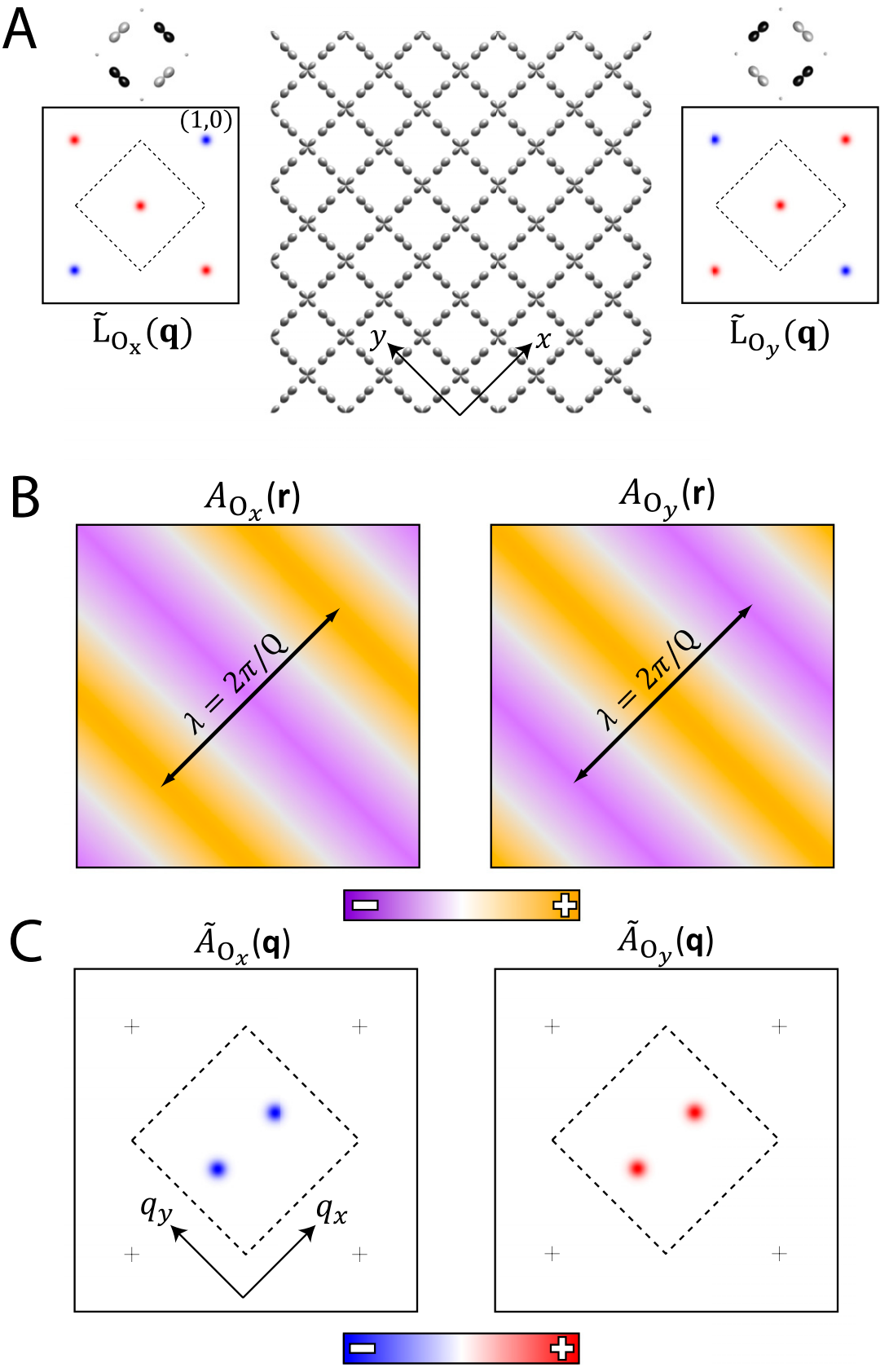

Fig. S3. Sublattice decomposition of *d*-form factor DW. (*A*) Fourier transforms of the *x*-bond and *y*-bond oxygen sublattices without a DW modulation. Gray orbitals signify those in the sublattice under consideration and black those in the other sublattice. (*B*) Schematic of continuous functions $A_{O_{x,y}}(\boldsymbol{r})$ that when multiplied by the sublattice functions $L_{O_{x,y}}(\boldsymbol{r})$ yield density waves in antiphase on the two sublattices with a modulation along the *x* direction. (*C*) Fourier transforms of the functions $A_{O_{x,y}}(\boldsymbol{r})$ exhibiting a relative phase of π as required for a *d*-form factor density wave.

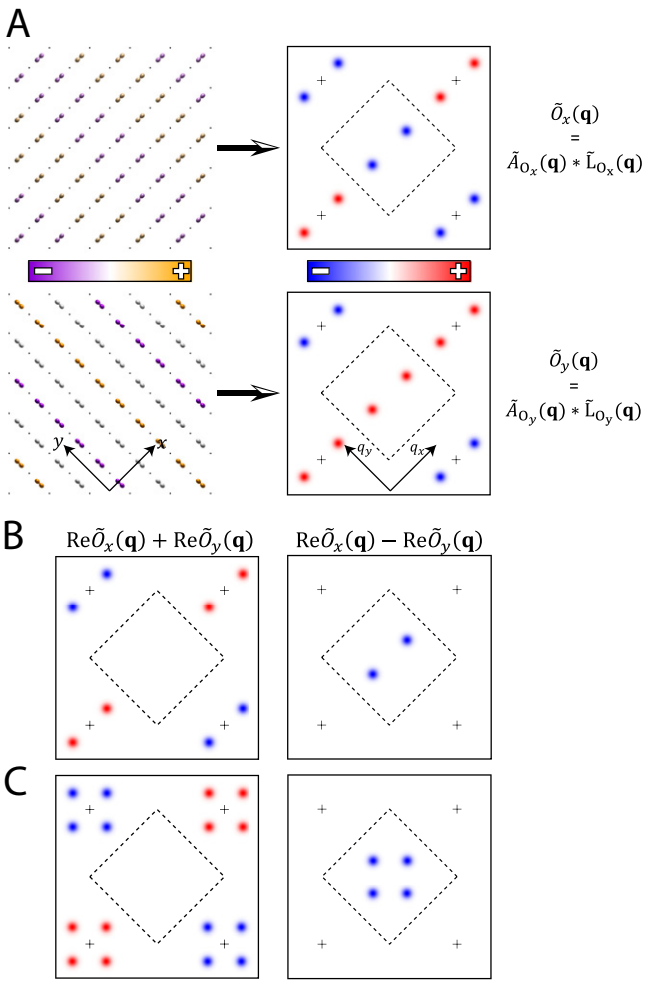

Fig. S4. Fourier analysis of DW using the convolution theorem. (*A*) Schematic of the segregated sublattice images $O_{x,y}(\boldsymbol{r})$ and their Fourier transforms $\tilde{O}_{x,y}(\boldsymbol{q})$ that can be obtained from Fig. S3 by application of the convolution theorem. (*B*) Sum and difference of $Re\tilde{O}_x(\boldsymbol{q})$ and $Re\tilde{O}_y(\boldsymbol{q})$ for a *d*-form factor density wave with modulation along the *x* direction at $\boldsymbol{Q} = (Q,0)$. Note that the origin of coordinates in real space has been chosen such that the Fourier transforms are purely real. (*C*) Sum and difference of $Re\tilde{O}_x(\boldsymbol{q})$ and $Re\tilde{O}_y(\boldsymbol{q})$ for a *d*-form factor density wave with modulations along the *x* and *y* directions at $\boldsymbol{Q} = (Q,0),(0,Q)$. The key signature of the *d*-form factor is the absence of the peaks at $(Q,0),(0,Q)$ in $Re\tilde{O}_x(\boldsymbol{q}) + Re\tilde{O}_y(\boldsymbol{q})$ and their presence in $Re\tilde{O}_x(\boldsymbol{q}) - Re\tilde{O}_y(\boldsymbol{q})$; the converse is true for the DW peaks surrounding (±1, 0) and (0, ±1).

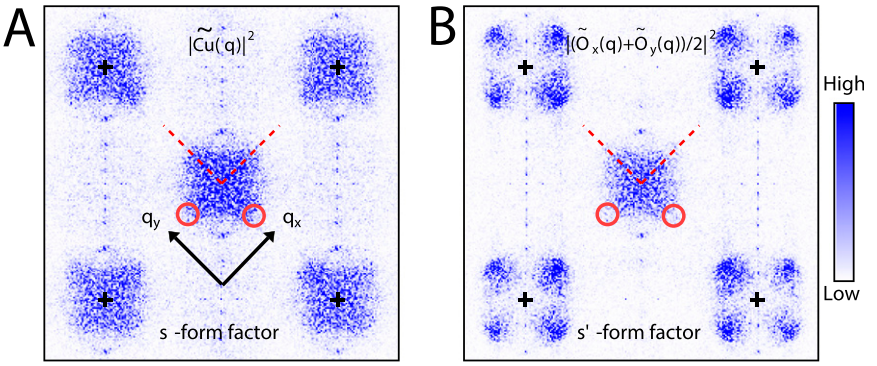

Fig. S5. Measurement of *s*-symmetry and *s*′-symmetry form factors. (*A*) PSD Fourier transform of $R(\boldsymbol{r})$ measured only at Cu sites, yielding $|\widetilde{Cu}(\boldsymbol{q})|^2$. This provides the measure of relative strength of the *s*-form factor in the DW. (*B*) PSD Fourier transform of $R(\boldsymbol{r})$ measured only at O_x/O_y sites, yielding $|(\tilde{O}_x(\boldsymbol{q}) + \tilde{O}_y(\boldsymbol{q}))/2|^2$. This provides the measure of relative strength of the *s*′-form factor in the DW.

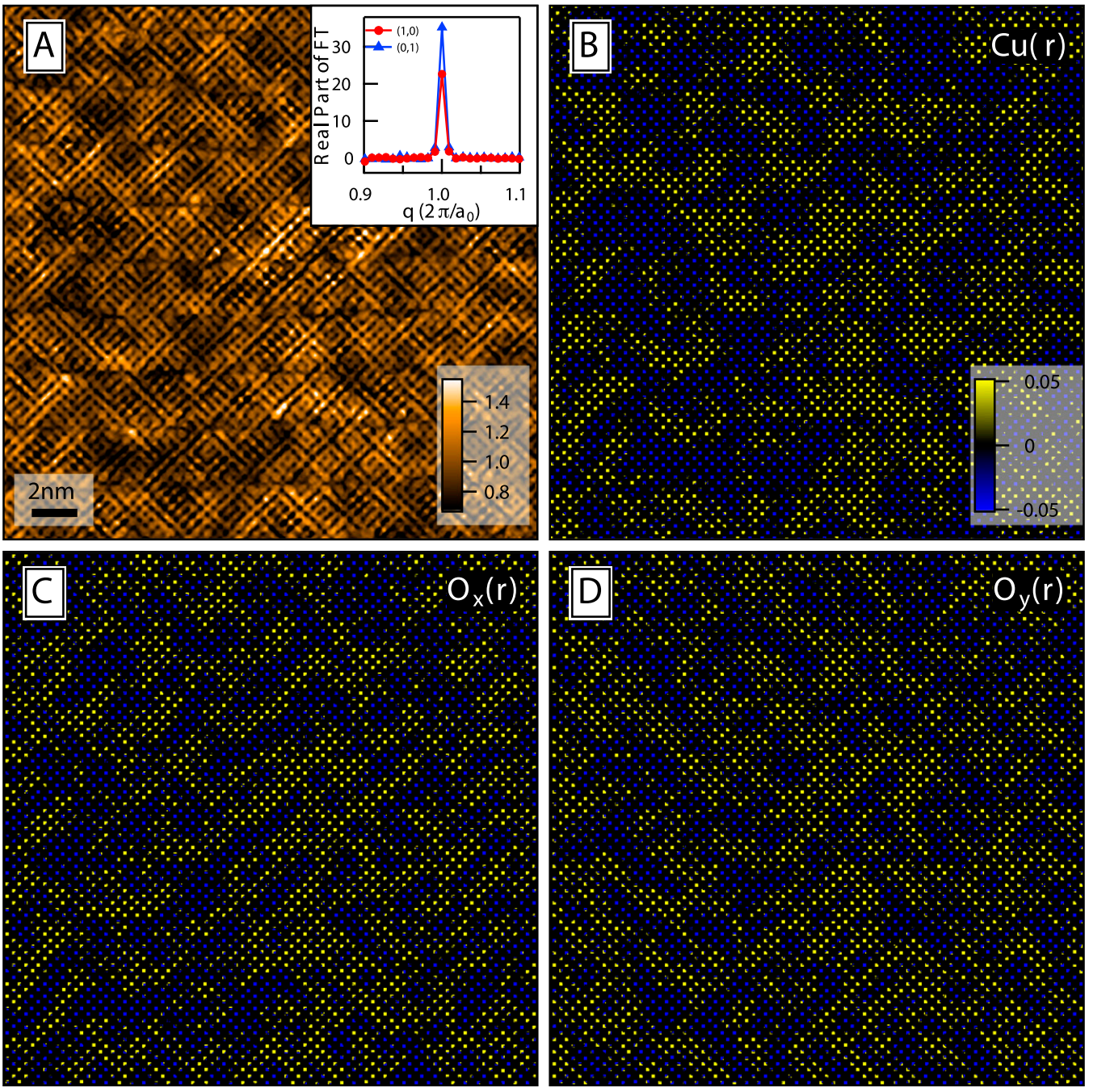

Fig. S6. Sublattice segregation for BSCCO. (*A*) Measured $R(\boldsymbol{r})$ for BSCCO sample with $p \sim 8 \pm 1\%$. These data are a subset of Fig. 2*A* in the main text reproduced here for clarity. *Inset* demonstrates an inequivalence between the real component of Bragg intensity for (1,0) and (0,1) peaks in the Fourier transforms of the electronic structure image before sublattice segregation, signaling a $\boldsymbol{Q} = 0$ nematic state. (*B*) Copper site segregated image, $Cu(\boldsymbol{r})$, in which the spatial average is subtracted, with copper sites selected from *A*. (*C*) *x*-bond oxygen-site segregated image, $O_x(\boldsymbol{r})$, in which the spatial average is subtracted, with *x*-oxygen sites selected from *A*. (*D*) *y*-bond oxygen-site segregated image, $O_y(\boldsymbol{r})$, in which the spatial average is subtracted, with *y*-oxygen sites selected from *A*.

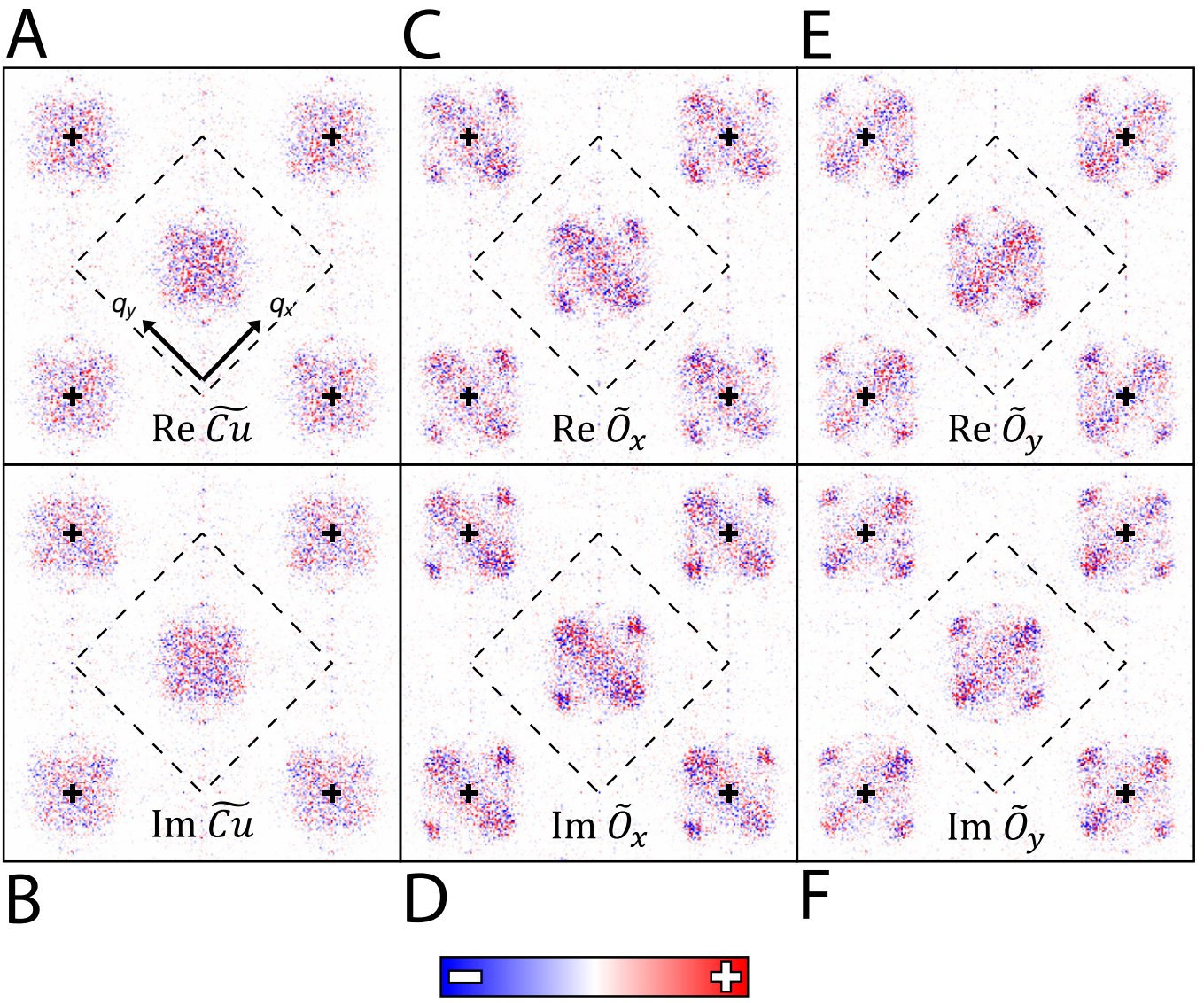

Fig. S7. Sublattice phase-resolved Fourier analysis for BSCCO. (*A*) Measured $Re\widetilde{Cu}(\boldsymbol{q})$ for BSCCO sample in Fig. 2*A* of the main text. No DW peaks are discernable at $\boldsymbol{Q} = (Q,0),(0,Q)$ or at Bragg satellites surrounding (±1, 0) and (0, ±1). This indicates a very small *s*-wave component for the density wave form factor. (*B*) Measured $Im\widetilde{Cu}(\boldsymbol{q})$ that also indicates a very small *s*-wave component. (*C*) Measured $Re\tilde{O}_x(\boldsymbol{q})$ showing DW peaks at $\boldsymbol{Q} = (Q,0),(0,Q)$ and corresponding Bragg satellites. (*D*) Measured $Im\tilde{O}_x(\boldsymbol{q})$ that exhibits the same structure as *C*. The strong overall phase disorder is apparent in the color variation within the DW peaks. (*E*) Measured $Re\tilde{O}_y(\boldsymbol{q})$ that also shows DW peaks at $\boldsymbol{Q} = (Q,0),(0,Q)$ along with Bragg satellites. (*F*) Measured $Im\tilde{O}_y(\boldsymbol{q})$ that exhibits the same structure as *E*.

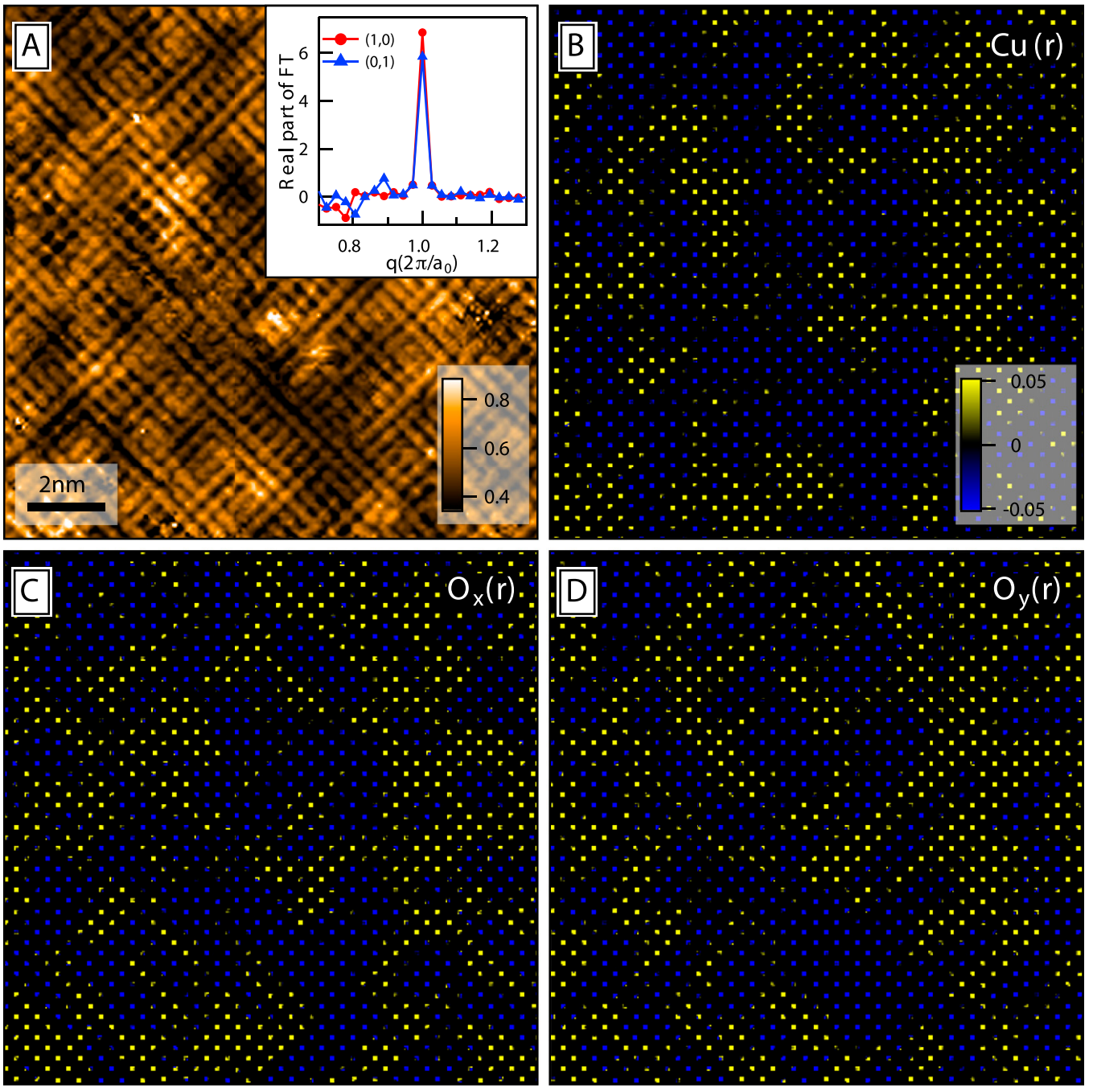

Fig. S8. Sublattice segregation for NaCCOC. (*A*) Measured $Z(\boldsymbol{r},E = 150$ mV) for NaCCOC sample with $p \sim 12 \pm 1\%$. *Inset* demonstrates an inequivalence between the real component of Bragg intensity for (1,0) and (0,1) peaks in the Fourier transforms of the electronic structure image before sublattice segregation signaling a $\boldsymbol{Q} = 0$ nematic state, as in Fig. S6*A*. (*B*) Copper site segregated image, $Cu(\boldsymbol{r})$, in which spatial average is subtracted, with copper sites selected from *A*. (*C*) *x*-bond oxygen-site segregated image, $O_x(\boldsymbol{r})$, in which the spatial average is subtracted, with *x*-oxygen sites selected from *A*. (*D*) *y*-bond oxygen-site segregated image, $O_y(\boldsymbol{r})$, in which the spatial average is subtracted, with *y*-oxygen sites selected from *A*.

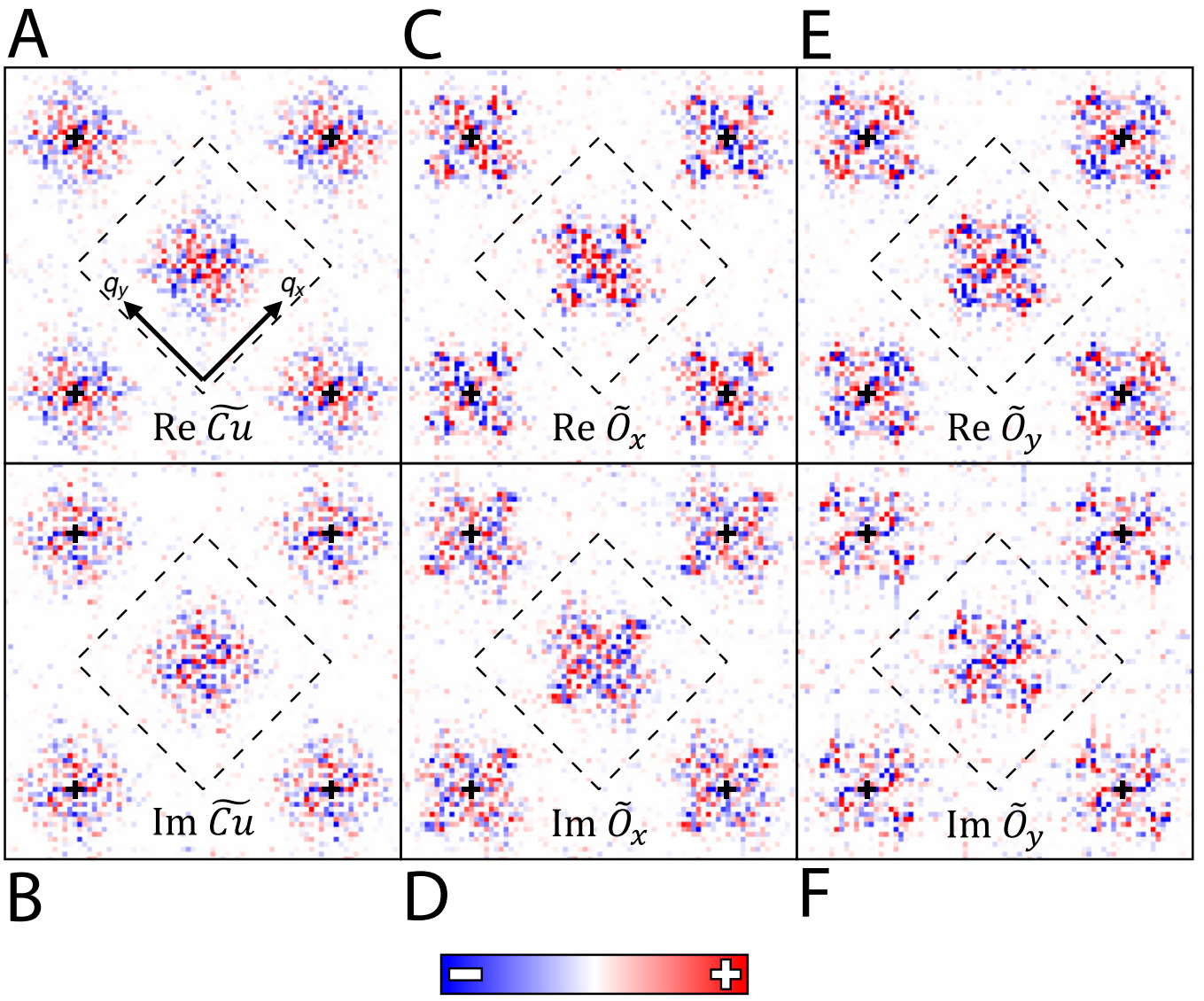

Fig. S9. Sublattice phase-resolved Fourier analysis for NaCCOC. (*A*) Measured $Re\widetilde{Cu}(\boldsymbol{q})$ for NaCCOC sample with $p \sim 12 \pm 1\%$. No DW peaks are discernable at $\boldsymbol{Q} = (Q,0),(0,Q)$ or at Bragg satellites surrounding $(\pm 1, 0)$ and $(0, \pm 1)$. This indicates that the DW in NaCCOC has, like BSCCO, a very small *s*-wave component in its form factor. (*B*) Measured $Im\widetilde{Cu}(\boldsymbol{q})$ that also indicates a very small *s*-wave component. (*C*) Measured $Re\tilde{O}_x(\boldsymbol{q})$ showing DW peaks at $\boldsymbol{Q} = (Q,0),(0,Q)$ and corresponding Bragg satellites. (*D*) Measured $Im\tilde{O}_x(\boldsymbol{q})$ that exhibits the same structure as *C*. The color variation within the DW peaks is smaller for NaCCOC than for BSCCO, indicating a less disordered DW. (*E*) Measured $Re\tilde{O}_y(\boldsymbol{q})$ that also shows DW peaks at $\boldsymbol{Q} = (Q,0),(0,Q)$ along with Bragg satellites. (*F*) Measured $Im\tilde{O}_y(\boldsymbol{q})$ that exhibits the same structure as *E*.

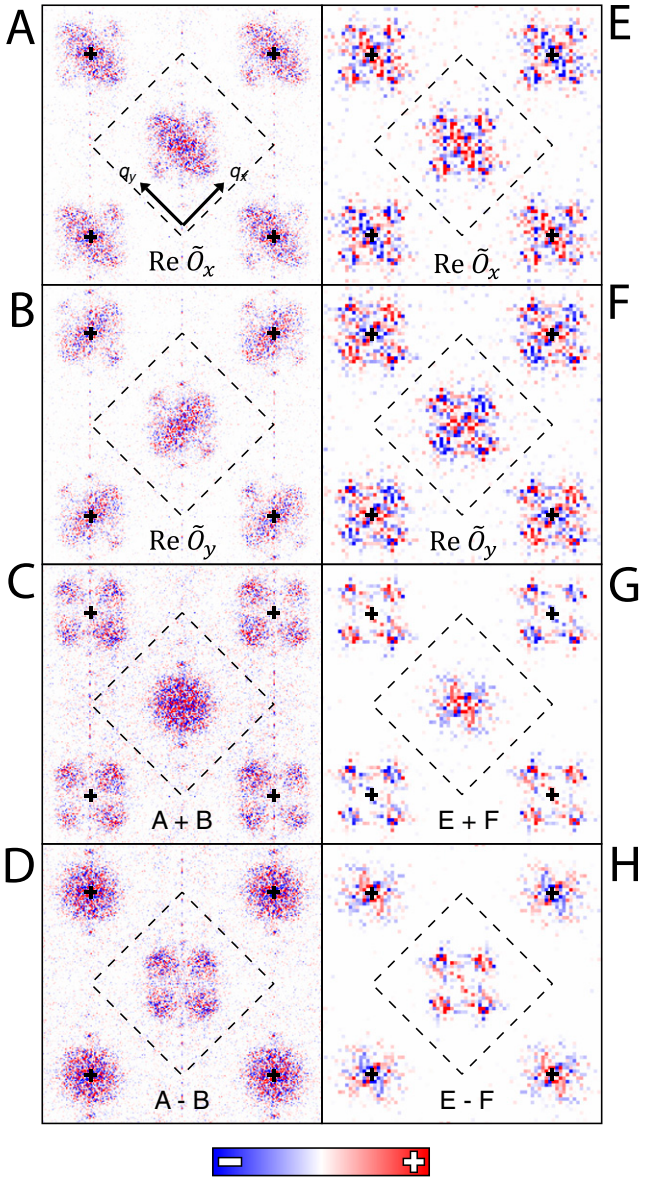

Fig. S10. Comparison of $Z(\mathbf{r},E = 150$ meV) between BSCCO and NaCCOC. (*A*) Measured $\tilde{O}_x(\mathbf{q})$ for BSCCO sample with $p \sim 8 \pm 1\%$ obtained using $Z(\mathbf{r},|E|) = g(\mathbf{r},E)/g(\mathbf{r},-E)$, $E = 150$ meV. (*B*) Measured $\tilde{O}_y(\mathbf{q})$ for BSCCO sample using the same analysis as in *A*. (*C*) Measured $Re\tilde{O}_x(\mathbf{q}) + Re\tilde{O}_y(\mathbf{q})$ from *A* and *B*. The absence of the four DW peaks at $\mathbf{Q}$ is characteristic of a *d*-form factor DW. (*D*) Measured $Re\tilde{O}_x(\mathbf{q}) - Re\tilde{O}_y(\mathbf{q})$ from *A* and *B*. The presence of the four DW peaks at $\mathbf{Q}$ and absence of the Bragg satellite peaks are another expectation for a *d*-form factor DW. (*E*) Measured $\tilde{O}_x(\mathbf{q})$ for NaCCOC sample with $p \sim 12 \pm 1\%$ obtained using $Z(\mathbf{r},|E|) = g(\mathbf{r},E)/g(\mathbf{r},-E)$, $E = 150$ meV. (*F*) Measured $\tilde{O}_y(\mathbf{q})$ for NaCCOC sample using the same analysis as in *E*. (*G*) Measured $Re\tilde{O}_x(\mathbf{q}) + Re\tilde{O}_y(\mathbf{q})$ from *E* and *F*. The same key signature of a *d*-form factor DW is present in this measurement of NaCCOC as is present in that for BSCCO in *C*. (*H*) Measured $Re\tilde{O}_x(\mathbf{q}) - Re\tilde{O}_y(\mathbf{q})$ from *E* and *F*. The signatures of a *d*-form factor DW are once again seen for NaCCOC in this image and should be compared with that for BSCCO in *D*.